AGU PUBLICATIONS

JGR

Journal of Geophysical Research: Oceans

RESEARCH ARTICLE

10.1002/2016JC011647

Key Points:

- Vertical flux of heat due to mean ocean circulation diagnosed from observations
- Diagnosed flux is consistent with results from a coupled GCM simulation
- Vertical heat transport dominated globally by downward contribution from Southern Ocean

Supporting Information:

- Supporting Information S1

Correspondence to:

P. Cummins,
Patrick.Cummins@dfo-mpo.gc.ca

Citation:

Cummins, P. F., D. Masson, and O. A. Saenko (2016), Vertical heat flux in the ocean: Estimates from observations and from a coupled general circulation model, *J. Geophys. Res. Oceans*, *121*, 3790–3802, doi:10.1002/2016JC011647.

Received 14 JAN 2016
Accepted 18 APR 2016
Accepted article online 21 APR 2016
Published online 3 JUN 2016

Vertical heat flux in the ocean: Estimates from observations and from a coupled general circulation model

Patrick F. Cummins[1], Diane Masson[1], and Oleg A. Saenko[2]

[1]Institute of Ocean Sciences, Fisheries and Oceans Canada, Sidney, British Columbia, Canada, [2]Canadian Centre for Climate Modelling and Analysis, Environment and Climate Change Canada, Victoria, British Columbia, Canada

Abstract The net heat uptake by the ocean in a changing climate involves small imbalances between the advective and diffusive processes that transport heat vertically. Generally, it is necessary to rely on global climate models to study these processes in detail. In the present study, it is shown that a key component of the vertical heat flux, namely that associated with the large-scale mean vertical circulation, can be diagnosed over extra-tropical regions from global observational data sets. This component is estimated based on the vertical velocity obtained from the geostrophic vorticity balance, combined with estimates of absolute geostrophic flow. Results are compared with the output of a non-eddy resolving, coupled atmosphere-ocean general circulation model. Reasonable agreement is found in the latitudinal distribution of the vertical heat flux, as well as in the area-integrated flux below about 250 m depth. The correspondence with the coupled model deteriorates sharply at depths shallower than 250 m due to the omission of equatorial regions from the calculation. The vertical heat flux due to the mean circulation is found to be dominated globally by the downward contribution from the Southern Hemisphere, in particular the Southern Ocean. This is driven by the Ekman vertical velocity which induces an upward transport of seawater that is cold relative to the horizontal average at a given depth. The results indicate that the dominant characteristics of the vertical transport of heat due to the mean circulation can be inferred from simple linear vorticity dynamics over much of the ocean.

1. Introduction

The uptake of heat by the ocean accounts for over 90% of the additional heating of the earth associated with anthropogenic greenhouse gas emissions [*Otto et al*., 2013], contributing importantly, through thermal expansion of seawater, to global sea level rise [*Church et al*., 2013]. Such changes in oceanic heat content arise as small residual imbalances between the advective and diffusive processes that transport heat vertically in the ocean. The dominant balances that govern the vertical transport of heat have been discussed for many decades. In a paradigmatic study, *Munk* [1966] proposed a diapycnal advective-diffusive balance such that sinking of cold water at high latitudes is balanced by the downward diffusion of heat through small-scale turbulent mixing, uniformly distributed over the abyssal ocean. This balance was later reinterpreted by *Munk and Wunsch* [1998] in terms of concentrated sources of buoyancy flux along oceanic margins.

In recent years, a number of studies with ocean general circulation models (GCMs) have suggested that the vertical transport of heat is dominated globally by a fundamentally different balance. Using a coarse resolution, coupled atmosphere-ocean GCM, *Gregory* [2000] found that, in a globally integrated sense, the time mean circulation of the ocean transports heat downward at all depths. Below the surface layer, this downward transport was largely balanced by the modeled upward diffusion of heat along isopycnal surfaces, with Southern Ocean upwelling playing a key role in this process. *Gnanadesikan et al*. [2005] considered the energetics of the buoyancy budget and argued that the downward flux of heat due to the mean circulation is driven by pressure work done by the wind on surface geostrophic currents.

These coarse resolution model results were supported in the global, eddy-permitting simulation discussed by *Wolfe et al*. [2008] who showed that downward transport of heat by the mean circulation was largely balanced by the upward transport of heat by the resolved eddy fluxes. Recently, *Griffies et al*. [2015] evaluated the eddy heat transport in coupled atmosphere-ocean GCMs at three different horizontal resolutions. In a coarse resolution model, the downward transport of heat by the large-scale mean circulation was balanced by parameterized eddy fluxes that induce an upward flux on isopycnal surfaces. In the eddy-permitting simulations, the dominant balance below the surface mixed layer was found to be between the downward heat transport associated with the time-mean circulation and the upward heat transport driven by transient eddies. These global model results are also supported by *Morrison et al*. [2013], who were able to run their idealized-basin, eddy-permitting model for 2500 years to near-equilibrium.

To date, the global vertical heat transport has been considered almost exclusively in terms of GCM simulations. One exception is the recent study of *Liang et al*. [2015] that presents results on the vertical heat budget from a 20 year state estimate with the data assimilating ECCO II model. They found that spatial patterns of vertical heat exchange were largely determined by advective rather than diffusive processes.

In the present study, global observational data sets are used to estimate the vertical heat flux in the ocean associated with the mean circulation. This estimate is based on the geostrophic vorticity balance which is used to diagnose the large-scale, time-mean vertical circulation. Observations of drift at depth from Argo floats are used to constrain the meridional geostrophic flow in this balance. The results are shown to capture the salient features of the vertical heat flux in a simulation with a non-eddying, coupled atmosphere-ocean GCM. The sensitivity of the results to different assumptions is also examined.

The next section presents the approach taken to compute the heat flux. Details on the GCM simulation are given in section 3. Estimates of the vertical heat flux inferred from observations along with sensitivity tests are presented in section 4. The concluding section summarizes the main findings and discusses implications of the results.

2. Calculation of Vertical Heat Flux

The area-integrated, time-averaged flux of heat due to vertical advection in the ocean is given by $H_a(z)=\int\int c\,\overline{wT}\,dA=c\langle\overline{wT}\rangle$, where w is the vertical velocity, T is the potential temperature and c, the volumetric heat capacity of seawater, is taken as a constant. The overbar denotes a time average, and the angle brackets represent an integration over the entire horizontal surface of the ocean at a given depth, z. Partitioning into time-averaged and fluctuating components, we have $H_a(z)=H_m(z)+H_e(z)$, where

$$H_m(z)=c\langle\overline{w}\,\overline{T}\rangle \tag{1}$$

is the net advective transport of heat due to the mean circulation, and $H_e(z)=c\langle\overline{w'T'}\rangle$ is the eddy-induced component of the vertical advective flux of heat, with primes denoting fluctuations about the time mean. In this study, we are concerned with evaluating $H_m(z)$. Consequently, in the following, the overbar is dropped and it is implicit that all variables are time-averaged quantities.

It is useful to write (1) as $H_m(z)=c\langle(A^{-1}\langle w\rangle+w^*)(A^{-1}\langle T\rangle+T^*)\rangle$, where the asterisk denotes the departure, at any point, from the level mean and $A(z)$ is the area of the ocean at a given depth. Expanding gives

$$H_m(z)=c\left[A^{-1}\langle w\rangle\,\langle T\rangle+\langle w^*A^{-1}\langle T\rangle\rangle+\langle T^*A^{-1}\langle w\rangle\rangle+\langle w^*T^*\rangle\right]$$

Since $\langle\langle w\rangle T^*\rangle=\langle\langle T\rangle w^*\rangle=0$, this simplifies to,

$$H_m(z)=c\,A^{-1}\langle w\rangle\,\langle T\rangle+c\langle w^*T^*\rangle.$$

Mass conservation requires that $\langle w\rangle=0$ at every depth. As a result, (1) reduces to,

$$H_m(z)=c\langle w^*T^*\rangle=\langle h_m\rangle. \tag{2}$$

The heat flux per unit area, $h_m(\lambda,\theta,z)=c\,w^*\,T^*=c\,w\,T^*$, represents the nonvanishing contribution to the net vertical heat flux at each point on a given vertical level, with λ and θ the longitudinal and latitudinal coordinates, respectively. This quantity, in particular its zonal integral, will be examined to assess the dominant spatial features of heat flux associated with the mean circulation. As described below, global observational data sets are used to infer the vertical velocity and the potential temperature anomaly, $T^*=(T-A^{-1}\langle T\rangle)$, through the water column. These estimates are compared with similar calculations based on results from an extended simulation with a coupled atmosphere-ocean GCM.

While mass conservation is strictly maintained in the GCM, there is no assurance that the vertical velocity diagnosed from observations will identically satisfy the constraint $\langle w \rangle = 0$. However, the prior removal of the area-averaged potential temperature, such that $c\langle wT^* \rangle$ is calculated directly (rather than $c\langle wT \rangle$), ensures that any nonzero residual in the area-averaged vertical velocity makes no contribution to the net heat flux at any depth.

2.1. Estimation of Vertical Velocity

Geostrophic motions in the ocean occurring on scales that are large compared to those of synoptic eddies are governed to lowest order by the geostrophic vorticity balance [*Pedlosky*, 1987],

$$f\frac{\partial w}{\partial z} = \beta v_g, \tag{3}$$

where v_g is the meridional component of geostrophic velocity, $f = 2\Omega\sin\theta$ is the Coriolis parameter and $\beta = 2\Omega\cos\theta/R$ is its latitudinal gradient with R, the radius of the earth, and Ω, the earth's angular rate of rotation. The balance in (3) represents a linearization of the vorticity equation such that vortex stretching balances northward advection of planetary vorticity. Given an estimate of the geostrophic velocity, it may be used to diagnose the large-scale vertical velocity field, except in immediate proximity of the equator.

Thomas et al. [2014] recently examined the validity of the geostrophic vorticity balance in a 15 year average state estimate from the ECCO-GODAE model. Overall, a close correspondence in the large-scale patterns of the two terms in (3) was evident in the upper ocean. Residual terms in the vorticity equation associated with advection and horizontal viscosity were typically an order of magnitude smaller than the terms in (3), and of relatively small scale, particularly at higher latitudes and over western boundary currents. It is worth noting that abyssal flows may be poorly represented by (3) due to neglect of a bottom pressure torque associated with the kinematic bottom boundary condition [*Lu and Stammer*, 2004].

Vertical integration of (3) from the base of the Ekman layer, z_e, to depth z yields,

$$w(z) = w_e - \frac{\beta}{f}\int_z^{z_e} v_g(z')dz', \tag{4}$$

where w_e is the Ekman vertical velocity. The latter is obtained here using surface wind stress data from atmospheric reanalysis products. The geostrophic velocity in (4) is determined through vertical integration of the thermal wind relation,

$$v_g(z) = v_g(z_0) + \frac{g}{\rho_o f R\cos\theta}\int_z^{z_0} \frac{\partial\rho}{\partial\lambda}dz', \tag{5}$$

where ρ_0 is a constant reference density, g is the acceleration of gravity, and ρ is the observed potential density field, available from climatological atlases. The geostrophic velocity at a reference depth, z_0, is needed to determine $v_g(z)$. The traditional approach to this problem is to postulate a deep level of no motion. However, deep ocean transports are sensitive to this assumption which has been shown to be inaccurate [e.g., *Pond and Pickard*, 1983]. In more modern approaches, the geostrophic circulation has been inferred using inverse methods applied to box models constrained by conservation laws and observations [e.g., *Ganachaud and Wunsch*, 2000]. As discussed below, data products have become available in recent years that allow specification of the absolute geostrophic velocity.

2.2. Observational Data Sets

Use is made of a number of global, or near-global, data sets to estimate the vertical heat flux according to the approach outlined above. The World Ocean Atlas 2013 (*Boyer et al*., 2013; hereinafter WOA13) is used to specify the potential temperature anomaly, $T^*(\lambda, \theta, z)$, and the climatological potential density field for the second term on the right hand side of (5), at a horizontal resolution of 1° with 102 levels in the vertical. Two sources of data were considered to obtain the Ekman vertical velocity: mean monthly surface stresses at a horizontal resolution of about 1.9° from the NCEP reanalysis [*Kalnay et al*., 1996], and at a resolution of 1° from ECMWF [*Dee et al*., 2011].

As mentioned above, data sets are available to specify the reference geostrophic velocity in (5). In particular, absolute geostrophic velocity is available from the AGVA (Absolute Geostrophic Velocities from Argo) data set prepared by *Gray and Riser* [2014]. This provides absolute geostrophic velocities through the upper 2000 m of the ocean at 1° resolution. The reference velocity is derived from a direct observational estimate of velocity at depth from the global array of Argo floats, using the horizontal drift of the floats at their deep "parking depth." In addition, absolute sea surface topography from the AVISO (Archiving, Validation and Interpretation of Satellite Oceanographic) altimeter data is available at a horizontal resolution of 1° [*AVISO*, 2011]. The meridional component of geostrophic velocity at the surface can then be determined as,

$$v_s = \frac{g}{fR\cos\theta}\frac{\partial\eta}{\partial\lambda}, \tag{6}$$

where η is the time-averaged sea level displacement relative to the earth's geoid. In terms of the present application, the merits of the AVISO and AGVA data sets are complementary. The AGVA data set provides values that may usefully constrain the solution at depth. Eddy noise is evident, however, in these data due to the relatively short duration of the records. On the other hand, the satellite data provide a smooth field of mean meridional velocity at the surface.

While ideally all the data sets used in the analysis should represent climatological means over a period of several decades, compromises, at times severe, are inevitable. The longest records are from the WOA13 and NCEP reanalysis and cover the period 1955–2012 and 1948-present, respectively. The ECMWF analyses are for a somewhat shorter period, 1979-present. The shortest records are the AVISO data and, especially, the AGVA data which extend for the 18 year period 1993–2010, and the 6 year period, 2005–2010, respectively.

3. Coupled Atmosphere-Ocean GCM

For comparison with observationally-based estimates, the vertical flux of heat was calculated from the results of an extended simulation with the Canadian Earth System Model (CanESM2) [see *Arora et al*., 2011, and references therein]. This model consists of coupled atmosphere and ocean GCMs, as well as sea-ice, land and carbon cycle models. As described in *von Salzen et al*. [2013], the atmospheric component of CanESM2 is a spectral model employing T63 triangular truncation with 35 vertical levels. The oceanic component of CanESM2 is based on the Modular Ocean Model [see *Yang and Saenko*, 2012, and references therein]. It has 40 vertical levels with a horizontal resolution of 1.41° and 0.94° in the zonal and meridional directions, respectively. Eddy fluxes in the model are represented using the *Gent and McWilliams* [1990] parameterization of mesoscale eddies, and the *Redi* [1982] isopycnal mixing scheme. The model also includes a parameterization of vertical mixing in the abyssal ocean due to rough topography [*Saenko and Merryfield*, 2005], following the approach outlined by *Simmons et al*. [2004].

The coupled model was run for more than 4000 years during which time concentrations of greenhouse gases were held fixed at their preindustrial levels. This run is an extension of the CanESM2 preindustrial control simulation conducted for the Coupled Model Intercomparison Project Phase 5 [*Taylor et al*., 2012]. Here we analyze a 20 year mean state of the ocean from this simulation obtained by averaging the quantities of interest (e.g., ocean potential temperature and vertical velocity) over model years 4201–4220. The product of these averaged quantities is used to form the vertical advective component of the heat flux associated with resolved motions in the ocean model. See *Kuhlbrodt et al*. [2015] for a discussion of resolved and parameterized advective fluxes, and the relation to diffusive fluxes.

4. Results

We consider first a basic case based on averages over the full period of the WOA13 data (1955–2012), and with the Ekman vertical velocity derived from the NCEP surface wind stresses over this same period. Sensitivity of the results to changes in the averaging period for the wind and hydrographic fields is considered in section 4.2. The AGVA data set, averaged over the period 2005–2010, is used to specify the reference geostrophic velocity in (5) at a depth of 900 m, a level that is close to the parking depth of most Argo floats. Use of the AGVA data set to specify the meridional flow directly into (4) over the entire upper 2000 m of the water column was also examined. This was found to yield results that are very similar to the basic case in

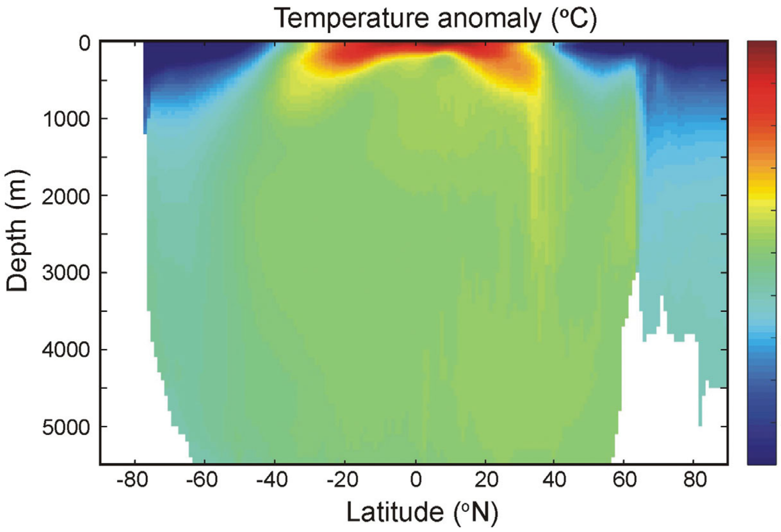

Figure 1. Zonal average of the long-term mean (1955–2012) spatial anomaly of potential temperature, T^*, from *World Ocean Atlas* [2013].

which the thermal wind relation is integrated using WOA13 data. Results are also presented below in which data from AGVA and AVISO are optimally combined to specify the reference geostrophic velocity in (5).

In all cases, the depth of the Ekman layer, z_e, is taken to be 50 m, the volumetric heat capacity, c, is set to a constant value of 4.1×10^6 J m^{-3} K^{-1}, and the potential temperature is determined with respect to surface pressure. Marginal seas and Arctic regions are excluded from the calculations. With respect to the latter, *Wolfe et al*. [2008] have noted that the net heat flux over the Arctic makes a negligible contribution to the global average, and can be safely excluded. This is also confirmed in results from the coupled GCM. In addition, the calculation of the vertical velocity was particularly noisy at a number of points located in the Arabian Basin and the Bay of Bengal of the North Indian Ocean. Rather than trying to eliminate a series of isolated points, these regions were simply excluded from the integration. Results from the GCM indicated that these regions make virtually no contribution to the zonally or globally integrated vertical heat flux.

The level mean potential temperature, $\langle T \rangle$, and the associated temperature anomaly, T^*, are calculated with respect to the actual area used in the horizontal integration of the heat flux. Exclusion of equatorial regions, the Arctic Ocean and other areas leads to negligible changes in $\langle T \rangle$ relative to an average over the entire area of the ocean; differences are no greater than 0.2°C below 125 m depth. The zonally averaged field of T^* calculated for the entire ocean is presented in Figure 1. This shows that large variations in T^*, on the order of ± 10°C, occur over the upper 1000 m. At greater depths, T^* is much smaller, particularly between 50°S and 60°N, which encompasses the great bulk of the ocean.

4.1. Basic Case

The temperature anomaly and the vertical velocity field obtained from (5) are presented in Figure 2 for a depth of 500 m. Similar fields drawn from the GCM simulation are presented for comparison. Both temperature anomaly fields are smooth and reflect the large-scale structure associated with the wind-driven gyres, and the Circumpolar Current. On the other hand, the vertical velocity fields vary over a greater range of spatial scales. This is especially the case for the field diagnosed from observations which has considerable small-scale structure at low latitudes. While there are numerous regional differences, a general consistency is nevertheless evident at large-scales between the model and the vertical velocity inferred from data, particularly with respect to the upward vertical velocity over the Southern Ocean. Also evident are the common patterns of sinking over subtropical latitudes and upwelling in subpolar regions.

Figure 3 compares the zonally integrated vertical transport derived from data and from the GCM. This quantity has units of m^{3}s^{-1} per degree of latitude, and is calculated as $Q(\theta_j, z) = R^2 \Delta\lambda \cos\theta_j \sum_i w(\lambda_i, \theta_j, z)$, where

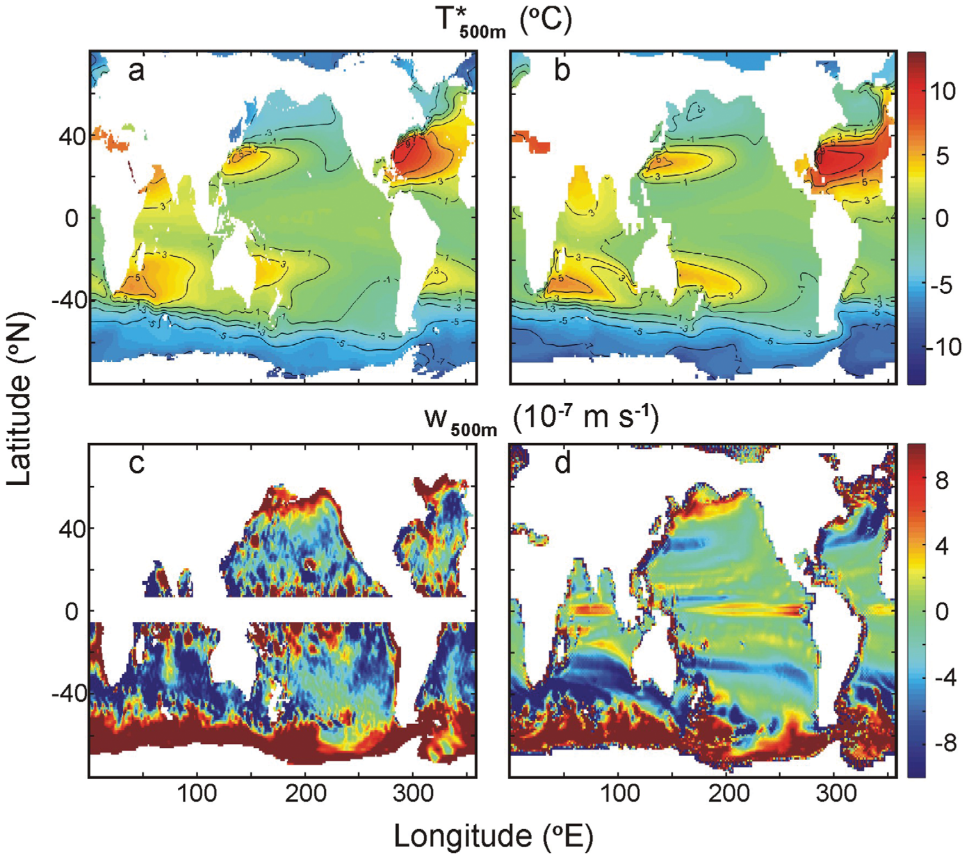

Figure 2. Potential temperature anomaly, T^* (°C), and vertical velocity, w (10^{-7} m s^{-1}), at 500 m depth diagnosed from (left) observations, and (right) the coupled GCM.

$(\lambda_i, \theta_j) = (i\Delta\lambda, j\Delta\theta)$, with $\Delta\lambda$ and $\Delta\theta$ the grid resolution in the zonal and meridional directions, respectively. The fields shown in Figure 3 are in reasonably good agreement, particularly over the Southern Hemisphere, where the vertical transport associated with the Deacon cell is dominant [e.g., *Döös and Webb*, 1994]. The diagnosed transport and GCM results both show the influence of the Ekman vertical velocity extending down to depths greater than 3000 m over the Southern Ocean and subpolar regions. In terms of the geostrophic vorticity balance, this must occur over the latitude range spanned by Drake Passage due to the absence of continental boundaries. As the net meridional geostrophic transport above the sill in Drake Passage vanishes, the zonal integral of (3) reduces to $\oint w(z)\,d\lambda = \oint w_e\,d\lambda$ for $z > -2000$ m. In fact, due to weak baroclinic pressure gradients, the influence of the Ekman vertical velocity extends below 2000 m depth and well beyond the latitude range of Drake Passage. On the other hand, baroclinic gradients are important equatorward of about 35°–40°S in the Southern Hemisphere and act to confine the downwelling associated with Ekman pumping to the upper 500 m of the water column. The integrated vertical transport is generally weaker over the Northern Hemisphere where the influence of Ekman pumping is evident over the subtropical gyre, down to about 500 m depth. The net upward transport over subpolar regions is small compared to the Southern Hemisphere.

Also notable in Figure 3 are regions where the vertical transport diagnosed from the geostrophic vorticity balance is at variance with the GCM results. In particular, the sinking at high latitudes evident in the GCM results is absent. The latter is driven by convective processes associated with the formation of Antarctic Bottom Water in the Southern Hemisphere and North Atlantic Deep Water (NADW) in the Northern Hemisphere. Such vertical motions are not represented by the linear vorticity balance (3). In addition, there are large diagnosed vertical transports in the deep ocean (depths $>$ 2000–3000 m), especially at low latitudes, that have no counterpart in the GCM results. Such motions are likely spurious; they arise from vertical integration of the noisy AGVA data used to specify the reference geostrophic velocity. The f^{-1} scaling

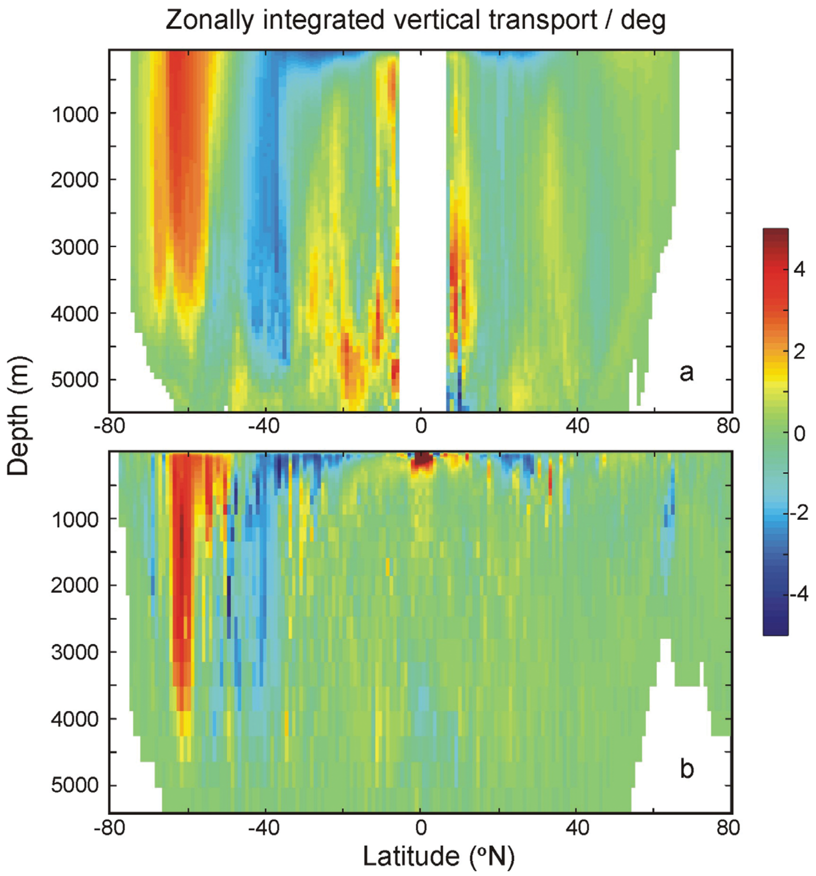

Figure 3. Zonally integrated vertical transport per degree of latitude (top) inferred from observations, and (bottom) calculated from the coupled GCM simulation. Units are Sverdrups (10^6 m^3 s^{-1}).

accentuates this noise near the equator. Lastly, near-surface equatorial upwelling is a notable feature that is evident in the GCM results of Figure 3, but omitted from the diagnosed field.

Figure 4 presents a comparison between the zonally integrated vertical heat flux from the coupled GCM and the field inferred from observations. This quantity has units of watts per degree of latitude, and is given by $\overline{h_m}(\theta_j, z)=R^2\Delta\lambda\cos\theta_j\sum_i h_m(\lambda_i, \theta_j, z)$. The total heat flux at a given depth is then $H_m(z)=\sum_j \Delta\theta\overline{h_m}(\theta_j, z)$. The results of Figure 4 indicate that the structure of the zonally integrated heat flux in the GCM is largely captured in the field derived from observations. In particular, the mean heat flux is dominated by the contribution from the Southern Hemisphere, especially the downward flux in the Southern Ocean which extends to depths of 3000–4000 m and is associated with the upwelling of Circumpolar Deep Water. Weaker, but still appreciable regions of downward flux extending to depths of 500–1000 m are associated with the subtropical gyres in both hemispheres. Due to the general attenuation of the temperature anomaly, T^*, with depth (Figure 1), the vertical heat flux in the Southern Hemisphere diminishes more quickly with depth than the vertical transport (Figure 2). In addition, the downwelling component of the Deacon cell makes only a weak contribution to the vertical heat flux, in contrast to the dominance of the upwelling component.

While the heat flux in Figure 4 is predominantly downward, regions of upward flux are also evident. In the GCM results, this is associated with deep water formation in polar regions and with divergence of the Ekman transport at the equator, leading to upwelling of anomalously warm water. The roughly 10°-wide band of upward heat flux centered at about 42°S is associated with the formation of Sub-Antarctic Mode Water, mainly through convective heat loss [*McCartney*, 1977; *Cerovečki et al.*, 2013]. This positive flux is captured, albeit weakly, in the diagnosed field as a result of the downward Ekman pumping of anomalously cool water. The diagnosed field also includes a pronounced upward flux centered at about 3000 m depth at low latitudes in the Northern Hemisphere (10°–15°N). This feature is associated with the spurious vertical velocity seen at depth in Figure 3a and likely meaningless.

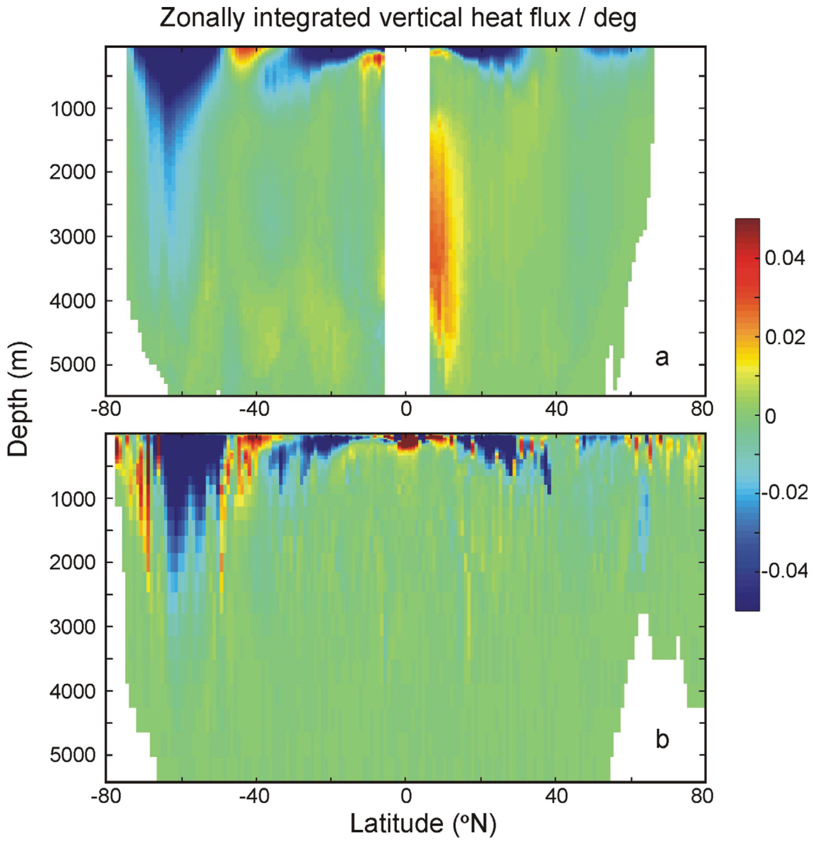

Figure 4. Zonally integrated vertical heat flux per degree of latitude (in PW) (top) inferred from observations, and (bottom) calculated from the coupled GCM simulation). Blue shading represents the downward transport of heat into the ocean.

The line plot of Figure 5 confirms that the structure of the downward heat flux diagnosed from observations is broadly consistent with the GCM results at different depths. Reasonable quantitative agreement is evident in the downward flux over the Southern Hemisphere. Conversely, the flux in the subtropical gyre of the Northern Hemisphere is larger in the GCM results than in the diagnosed field. Overall, this comparison indicates that the linear vorticity balance can be used to infer the most salient characteristics of the vertical heat flux associated with the large-scale mean circulation.

The globally integrated vertical heat fluxes based on observations are compared in Figure 6 with the GCM results. This comparison shows generally consistent behavior with a similar attenuation with depth below about 250 m depth. Equatorial regions, which are omitted in the diagnosed field, make a large positive contribution to the heat flux above this depth in the GCM results. The net downward heat flux associated with the time-averaged vertical circulation shown in Figure 6 is in approximate agreement with previously reported results from coarse resolution and eddy-permitting global models [*Gregory*, 2000; *Gnanadesikan et al*., 2005; *Wolfe et al*., 2008; *Griffies et al*., 2015]. While there is a remarkably close quantitative agreement below 250 m depth between the diagnosed flux and the GCM results, this may be somewhat fortuitous since in the GCM results there is some cancellation between the downward flux seen at most latitudes and the upward flux associated with deep water formation in the Southern Ocean. The latter is absent in the diagnosed field while the downward flux is somewhat weaker than in the GCM (Figures 4 and 5). The change in sign in the diagnosed field at about 3000 m depth is an artifact of the unphysical, positive flux seen at depth near the equator (Figure 4a).

4.2. Sensitivity Tests

In this section, we examine the sensitivity of the diagnosed vertical heat flux to changes in the averaging period for the Ekman vertical velocity, as well as for the hydrographic fields which control both the temperature

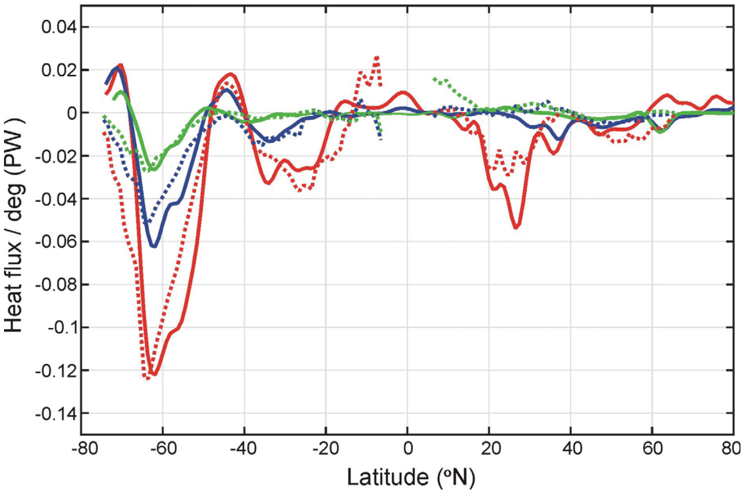

Figure 5. Zonally integrated heat flux per degree of latitude at depths of 300 m (red curves), 800 m (blue curves) and 1500 m (green curves) from the coupled GCM (solid lines), and diagnosed from observations (dashed lines). A Gaussian smoother with an e-folding scale of 2.5 grid intervals has been applied to the GCM results.

anomaly and the meridional velocity through the thermal wind relation. The influence of the data used to specify the reference geostrophic velocity is also considered.

4.2.1. Averaging Period

The upper panel of Figure 7 shows the variation in the zonally integrated heat flux at 300 m depth based on a series of decadal averages of the Ekman vertical velocity derived from the NCEP reanalysis wind stresses. Also included for comparison is the heat flux based on the long-term mean Ekman velocity from NCEP (1955–2012), and from the ECMWF (1979–2012) wind stresses. Hydrographic fields from the World Ocean Atlas are held fixed to the long-term mean (1955–2012) for each of these calculations. These results show that the vertical heat flux is relatively insensitive to the use of much shorter averaging periods for the wind forcing. Changes are largely confined to the Southern Ocean, where the peak downward heat flux shows some dependence on the averaging period. The results also demonstrate that replacement of long-term mean wind stresses from the NCEP reanalysis with those from ECMWF leads to relatively little change in the heat flux.

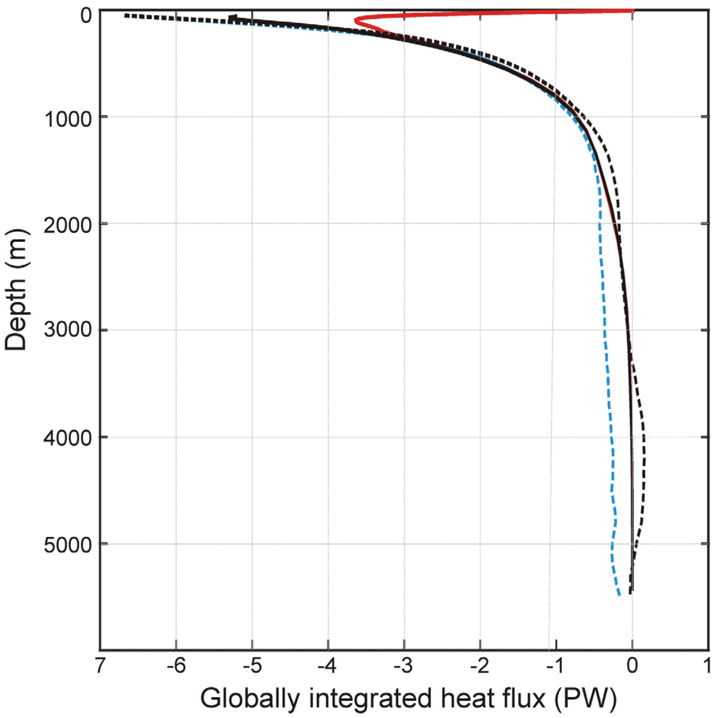

Figure 6. Depth dependence of the globally integrated vertical heat flux from the coupled GCM (red curve), the coupled GCM with the equatorial band omitted (solid black curve, plotted below 50 m depth), and inferred from observations in the basic case (dashed black curve). The dashed blue curve gives the observationally based estimate of the net heat flux for the case described in section 4.2.2 examining sensitivity to the reference geostrophic velocity.

The sensitivity to variations in the hydrographic fields used in the thermal wind relation and to specify T^* is examined in Figure 7b. Here the Ekman vertical velocity from NCEP is held constant to its long-term mean (1955–2012), and the hydrography from WOA13 is set to a series of decadal means (1955–1964, 1965–1974, etc.). The results show that the vertical heat flux is weakly sensitive to such variations, with changes limited mainly to subtropical regions of the Southern Hemisphere. Notably unaffected by variations in the hydrography is the globally dominant contribution to the heat flux over the Southern Ocean which is controlled by the wind forcing.

4.2.2. Reference Geostrophic Velocity

The sensitivity of the results to the data used to specify the

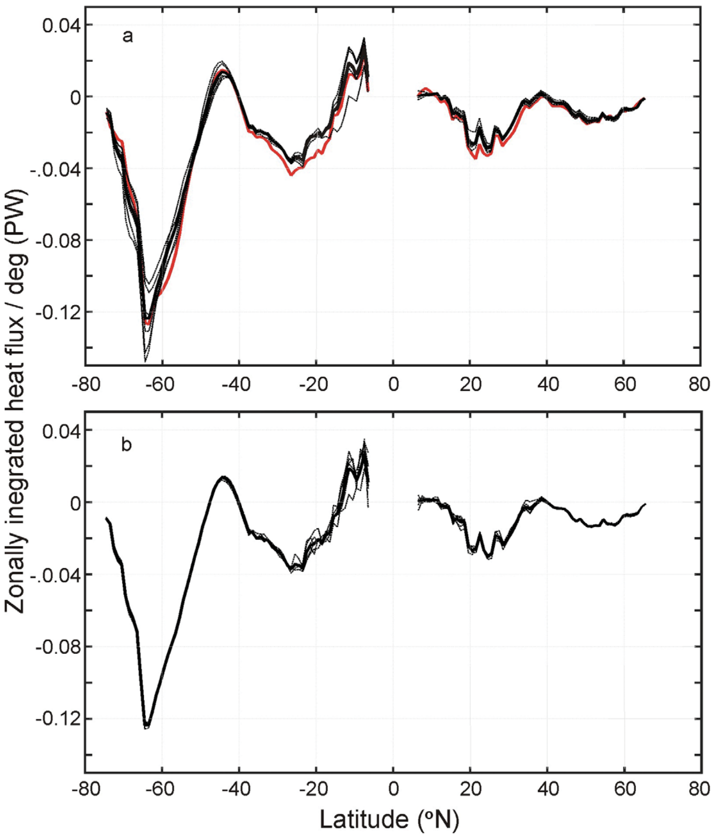

Figure 7. (a) Zonally integrated vertical heat flux at 300 m depth based on the long-term mean NCEP (thick black curve) and ECMWF (red curve) wind stresses. Thin black curves show the variation in the heat flux based on decadal averages of the NCEP wind stresses (i.e., averages over years 1955–1964, 1965–1974, . . ., 2005–2012). (b) Thin lines present the variation in the vertical heat flux at 300 m depth based on a similar set of decadal averages of WOA13 data. The thick line is based on the long-term mean WOA13 climatology (1955–2012).

reference geostrophic velocity is now considered. Here we use an alternative estimate of the geostrophic velocity obtained by optimally combining the AGVA and AVISO data to specify v_g at the surface. Accordingly, $v_0 \equiv v_g(z_0=0)$ in (5) is determined at each point by minimizing, in a least squares sense, the difference between observational estimates of v_g at the surface from AVISO and at 900 m depth from AGVA. A cost function is defined as,

$$J=\left(\frac{v_0-v_s}{\sigma_s}\right)^2+\left(\frac{v_0-(v_d-\delta)}{\sigma_d}\right)^2, \tag{7}$$

where v_s is given by (6), v_d is the meridional component of geostrophic velocity at 900 m depth, $\delta=\frac{g}{\rho_0 f R\cos\theta}\int_{-900\,\mathrm{m}}^{0}\frac{\partial\rho}{\partial\lambda}dz$ and $(\sigma_s,\ \sigma_d)$ are weights. Setting $\frac{\partial J}{\partial v_0}=0$ yields

$$v_0=\frac{v_s\sigma_d^2+(v_d-\delta)\sigma_s^2}{\sigma_s^2+\sigma_d^2}. \tag{8}$$

The weights in (7) are given a latitudinal dependence and are based on the mean square value of v_s and $(v_d-\delta)$ at each latitude for which data are available,

$$\left(\sigma_s^2(\theta),\sigma_d^2(\theta)\right)=\left(\frac{1}{N_s}\sum_{i=1}^{N_s}v_s^2,\ \frac{1}{N_d}\sum_{i=1}^{N_d}(v_d-\delta)^2\right). \tag{9}$$

This is the simplest form that allows for latitudinal variation in the magnitude of currents, which are larger in the Southern Ocean. Equation (8) is applied at each $1°\times1°$ grid point where meridional velocities from both AGVA and AVISO data are defined. There are a limited number of points over the Southern Ocean for which only AGVA data are available; for these, the surface reference velocity is taken as $v_0=(v_d-\delta)$.

Figure 8 presents the zonally integrated vertical transport and heat flux based on the use of (8) to specify the reference geostrophic velocity. Aside from the change in the reference velocity, the calculation is similar to the basic case discussed above. The results of Figure 8 may be compared with top panels of Figures 3 and 4 for the transport and heat flux, respectively. (The velocities v_s and v_d, along with the fitted values at the surface and at 900 m depth, are included in the supporting information.) With respect to the transport, it is clear that the change in reference velocity has substantially increased the spurious vertical motions found below 1000 m at low latitudes. In the Northern Hemisphere, this was found to be associated with regions in the western North Atlantic and western Pacific where there is an apparent incompatibility between the smoothed hydrography of WOA13 and the surface current derived from the AVISO. As a result, the meridional velocity is northward at all depths, rather than reversing to flow southward below 500–1000 m, as in the basic case. The integration of (5) then leads to strong sinking through most of the water column.

In contrast to the transport, the vertical heat flux shows much less sensitivity to the change in the reference velocity, due, in part, to the near horizontal homogeneity of the abyssal temperature field (Figure 1).

Some changes are nevertheless evident: the spurious positive flux centered at 3000 m depth at about 10°N (Figure 4, top) is almost entirely eliminated, while a weaker and equally questionable downward flux extending through much of the water column develops over a narrow band of latitudes centered at about 20°N (Figure 8, bottom). The globally integrated flux for this case, shown as the dashed blue curve in Figure 6, is virtually unchanged over the upper 1000–1500 m of the ocean. At greater depth, there is an offset from the basic case arising from the changes noted above in the deep fluxes in the Northern Hemisphere. Given this sensitivity, little confidence can be placed in the observationally based estimate below 2000 m depth.

5. Summary and Conclusions

The vertical flux of heat in the ocean involves a balance of terms associated with the mean circulation, eddy-induced fluxes, convection and small scale turbulent dissipation. Changes in oceanic heat storage result from small imbalances between these different processes. Generally, it is necessary to depend on global climate models to estimate the different contributing components to the vertical heat flux.

The results presented above show that, by combining atmospheric and oceanic data sets, it is possible to obtain an observationally based estimate of the component of the vertical heat flux associated with the mean circulation. The method is based on the geostrophic vorticity balance which is used to diagnose the climatological mean vertical velocity, given an estimate of the meridional component of absolute geostrophic velocity at a specified depth. This approach is subject to a number of limitations, most notably the omission of equatorial regions due to the singularity at the equator. Vertical motions driven by convection are also excluded.

Absolute geostrophic velocities from the AGVA data set [*Gray and Riser*, 2014] were found to be useful in constraining the vertical velocity field over the upper 1500 m of the water column over most of the ocean, and to greater depth over the Southern Ocean. Elsewhere the vertical velocity is poorly constrained in the abyss, particular at low latitudes, and the field tends to be noisy and dominated by large spurious values. This noise originates largely from vertical integration of the reference geostrophic velocity. While the reason(s) for this is not known, it seems plausible that the relatively short record associated with the AGVA data may be a factor contributing to the noisy vertical velocities in the deep ocean. On the other hand, blending these data with longer records of absolute geostrophic velocities from altimeter data did not improve matters, leading, in fact, to noisier results. The vertical heat flux above 1500–2000 m, however, is relatively insensitive to such uncertainties.

Comparisons with the mean vertical heat flux calculated from an extended simulation with a non-eddy resolving, coupled general circulation model demonstrate reasonably good agreement with the heat flux estimated from observations. Several common features are evident in the zonally integrated heat flux. In particular, the results demonstrate that the Southern Ocean makes the dominant contribution to the heat flux associated with mean circulation, in accordance with the results of *Gregory* [2000]. The largest signal, extending to over 3000 m depth, is the downward heat flux associated with the upwelling of Circumpolar Deep Water in the Southern Ocean. On the other hand, the contribution to the vertical heat flux associated with the downwelling branch of the Deacon cell is much weaker. Overall, the results are consistent with the emphasis placed by *Marshall and Speer* [2012] on the centrality of Southern Ocean upwelling to the climate system.

The subtropical gyres in both hemispheres make appreciable contributions to the vertical heat flux over the upper 500–1000 m of the water column. At depths shallower than 250 m, results from the GCM show that equatorial regions, which are excluded from the flux diagnosed from observations, make an important positive (i.e., upward) contribution to the area-integrated flux.

These results demonstrate that the Ekman vertical velocity is the dominant mechanism driving the heat flux associated with the mean circulation. As noted by *Griffies et al.* [2015], in the presence of a stabilizing vertical temperature gradient, wind-driven vertical motions produce an anticorrelation between temperature and vertical velocity, hence a downward flux of heat. Two exceptions to this process are evident in the results shown above. In the GCM, divergence of the Ekman transport at the equator leads to upwelling of water that is anomalously warm relative to the horizontal average, leading to an upward flux of heat that makes a globally significant contribution in the upper ocean. Second, the results indicate that convergence

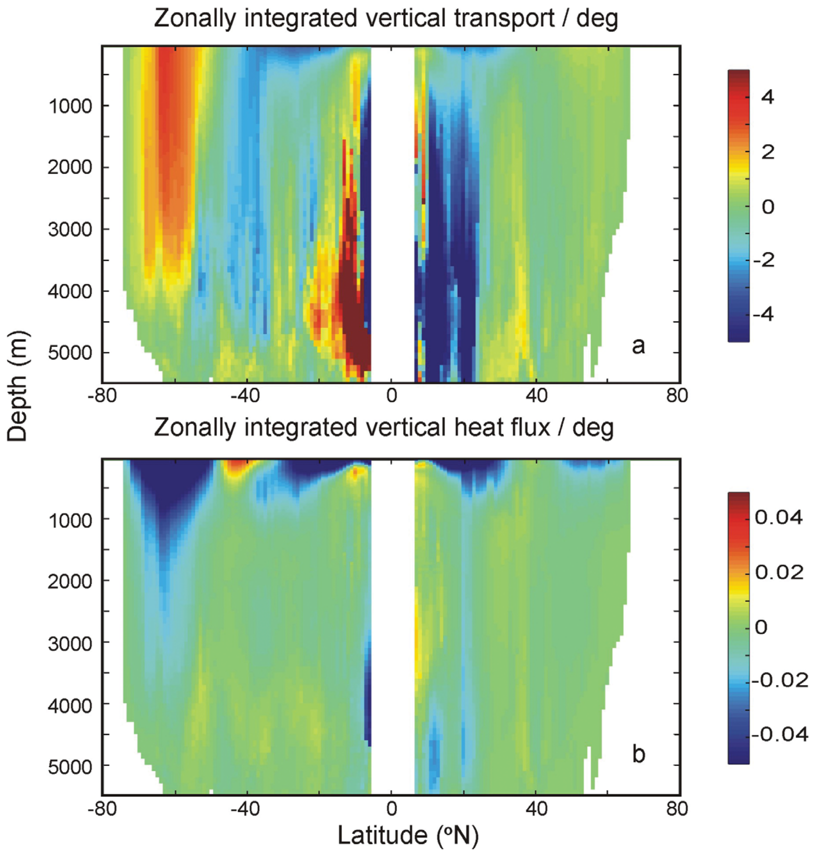

Figure 8. (a) Zonally integrated vertical transport (in Sv), and (b) heat flux (in PW) for the case discussed in section 4.2.2 in which AVISO and AGVA data are combined to specify the reference geostrophic velocity. Note that the large, spurious transports below 1000 m depth at low latitudes have relatively little influence on the heat flux.

of the Ekman transport over the formation region of Sub-Antarctic Mode Water contributes to the sinking of this anomalously cold water mass, with an attendant upward flux of heat. The time-averaged vertical velocity field from the GCM also reflects the sinking at high latitudes associated with convective processes. This produces an upward heat flux that is apparent in the zonally integrated field (Figure 4, bottom). This upward flux is, however, weak in comparison with the wind-driven downward flux.

Various advective and diffusive processes contribute to the vertical flux of heat in the ocean. This study represents a novel attempt to diagnose from global observational datasets the component of the flux associated with the mean circulation of the ocean. The resulting heat flux is quantitatively consistent with the flux associated with the mean circulation in a coarse resolution GCM simulation (e.g., Figure 5). Discrepancies between the two estimates can largely be explained by limitations of the method used to diagnose the flux from observations. As the dominant heat balance below the surface mixed layer in such coarse resolution models is between the upward flux due to parameterized eddies and the downward flux associated with the mean circulation, the agreement with the flux inferred from observations lends greater plausibility to the vertical heat fluxes in GCM simulations, including those associated with eddies.

Acknowledgments
The SLA data were distributed by AVISO and are publicly available at http://dx.doi.org/10.5067/DYNTO-1D1M1. The AGVA data are publicly available at http://flux.ocean.washington.edu/agva/. The World Ocean ATLAS 2013 version 2 data are available via https://www.nodc.noaa.gov/OC5/woa13/. NCEP Reanalysis Derived data are provided by the NOAA/OAR/ESRL PSD, Boulder, Colorado, USA, from their web site at http://www.esrl.noaa.gov/psd/. The ECMWF ERA-Interim data set was obtained via the ECMWF data server at http://apps.ecmwf.int/datasets.

References

Arora, V. K., J. F. Scinocca, G. J. Boer, J. R. Christian, K. L. Denman, G. M. Flato, V. V. Kharin, W. G. Lee, and W. J. Merryfield (2011), Carbon emission limits required to satisfy future representative concentration pathways of greenhouse gases, *Geophys. Res. Lett.*, *38*, L05805, doi:10.1029/2010GL046270.

AVISO (2011), AVISO Level 4 Absolute Dynamic Topography for Climate Model Comparison. Ver. 1. PO.DAAC, CA, USA. [Available at http://dx.doi.org/10.5067/DYNTO-1D1M1, last accessed 15 Jun. 2004.]

Boyer, T. P., et al. (2013), World Ocean Database 2013, NOAA Atlas NESDIS 72, edited by S. Levitus, and A. Mishonov, 209 pp., Silver Spring, Md., doi:10.7289/V5NZ85MT.

Cerovečki, I., L. D. Talley, M. R. Mazloff, and G. Maze (2013), Subantarctic mode water formation, destruction, and export in the eddy-permitting Southern Ocean state estimate, *J. Phys. Oceanogr.*, *43*, 1485–1511, doi:10.1175/JPO-D-12-0121.1.

Church, J. A., D. Monselesan, J. M. Gregory, and B. Marzeion (2013), Evaluating the ability of process based models to project sea-level change, *Environ. Res. Lett.*, *8*, 014051, doi:10.1088/1748-9326/8/1/014051.

Dee, D. P., et al. (2011), The ERA-Interim reanalysis: Configuration and performance of the data assimilation system, *Q. J. R. Meteorol. Soc.*, *137*, 553–597, doi:10.1002/qj.828.

Döös, K., and D. J. Webb (1994), The Deacon cell and other meridional cells of the Southern Ocean, *J. Phys. Oceanogr.*, *24*, 429–442.

Ganachaud, A., and C. Wunsch (2000), Improved estimates of global ocean circulation, heat transport and mixing from hydrographic data, *Nature*, *408*, 453–457, doi:10.1038/35044048.

Gent, P., and J. McWilliams (1990), Isopycnal mixing in ocean circulation models, *J. Phys. Oceanogr.*, *20*, 150–155, doi:10.1175/1520-0485.

Gnanadesikan, A., R. D. Slater, P. S. Swathi, and G. K. Vallis (2005), The energetics ocean heat transport, *J. Clim.*, *18*, 2604–2616, doi:10.1175/JCLI3436.1.

Gray, A. R., and S. C. Riser (2014), A global analysis of Sverdrup balance using absolute geostrophic velocities from Argo, *J. Phys. Oceanogr.*, *44*, 1213–1229, doi:10.1175/JPO-D-12-0206.1.

Gregory, J. M. (2000), Vertical heat transports in the ocean and their effect on time-dependent climate change, *Clim. Dyn.*, *16*, 501–515, doi:10.1007/s003820000059.

Griffies, S. M., et al. (2015), Impacts on ocean heat from transient mesoscale eddies in a hierarchy of climate models, *J. Clim.*, *28*, 952–977, doi:10.1175/JCLI-D-14-00353.1.

Kalnay, E., et al. (1996), The NCEP/NCAR 40-year reanalysis project, *Bull. Am. Meteorol. Soc.*, *77*, 437–470.

Kuhlbrodt, T., J. M. Gregory, and L. C. Shaffrey (2015), A process-based analysis of ocean heat uptake in an AOGCM with an eddy-permitting ocean component, *Clim. Dyn.*, *45*, 3205–3226, doi:10.1007/s00382-015-2534-0.

Liang, X., C. Wunsch, P. Heimbach, and G. Forget (2015), Vertical redistribution of oceanic heat content, *J. Clim.*, *28*, 3821–3833, doi:10.1175/JCLI-D-14-00550.1.

Lu, Y., and D. Stammer (2004), Vorticity balance in coarse-resolution global ocean simulations, *J. Phys. Oceanogr.*, *34*, 605–622., doi:10.1175/2504.1.

Marshall, J., and K. Speer (2012), Closure of the meridional overturning circulation through Southern Ocean upwelling, *Nat. Geosci.*, *5*, 171–180, doi:10.1038/NGEO1391.

McCartney, M. S. (1977), Subantarctic mode water, in *A Voyage of Discovery: George Deacon 70th Anniversary Volume*, edited by M. V. Angel, pp. 103–119, Pergamon, Oxford, U. K.

Morrison, A. K., O. A. Saenko, A. C. McHogg and P. Spence (2013), The role of vertical eddy flux in Southern Ocean heat uptake, *Geophys. Res. Lett.*, *40*, 5445–5450, doi:10.1002/2013GL057706.

Munk, W. (1966), Abyssal recipes, *Deep Sea Res. Oceanogr. Abstr.*, *13*, 707–730.

Munk, W., and C. Wunsch (1998), Abyssal recipes II: Energetics of tidal and wind mixing, *Deep Sea Res., Part I*, *45*, 1977–2010.

Otto, A., et al. (2013), Energy budget constraints on climate response, *Nat. Geosci.*, *6*, 415–416, doi:10.1038/ngeo1836.

Pedlosky, J. (1987), *Geophysical Fluid Dynamics*, 2nd ed., 710 pp., Springer, N. Y.

Pond, S., and G. L. Pickard (1983), *Introductory Dynamical Oceanography*, 2nd ed., 329 pp., Pergamon, Oxford, U. K.

Redi, M. H. (1982), Oceanic isopycnal mixing by coordinate rotation, *J. Phys. Oceanogr.*, *12*, 1154–1158.

Saenko, O. A., and W. J. Merryfield (2005), On the effect of topographically enhanced mixing on the global ocean circulation, *J. Phys. Oceanogr.*, *35*, 826–834.

Simmons, H. L., S. R. Jayne, L. C. St. Laurent, and A. J. Weaver (2004), Tidally driven mixing in a numerical model of the ocean general circulation, *Ocean Modell.*, *6*, 245–263.

Taylor, K. E., R. J. Stouffer, and G. A. Meehl (2012), An overview of CMIP5 and the experiment design, *Bull. Am. Meteorol. Soc.*, *93*, 485–498, doi:10.1175/BAMS-D-11-00094.1.

Thomas, M. D., A. M. De Boer, H. L. Johnson, and D. P. Stevens (2014), Spatial and temporal scales of Sverdrup balance, *J. Phys. Oceanogr.*, *44*, 2644–2660, doi:10.1175/JPO-D-13-0192.1.

von Salzen, K., et al. (2013), The Canadian fourth generation atmospheric global climate model (CanAM4). Part I: Representation of physical processes, *Atmos. Ocean*, *51*, 104–125, doi:10.1080/07055900.2012.755610.

Wolfe, C., P. Cessi, J. McClean, and M. Maltrud (2008), Vertical heat transport in eddying ocean models, *Geophys. Res. Lett.*, *35*, L23605, doi:10.1029/2008GL036138.

Yang, D., and O. A. Saenko (2012), Ocean heat transport and its projected change in CanESM2, *J. Clim.*, *25*, 8148–8163, doi:10.1175/JCLI-D-11-00715.1.